RSC Advances

PAPER

View Article Online
View Journal | View Issue

Check for updates

Cite this: *RSC Adv.*, 2026, **16**, 11284

Synthesis-route-regulated structural and electronic evolution of Fe-doped Co_3O_4 toward enhanced oxygen evolution reaction

Jian Lv, [ab] Hongtao Sun,[ab] Cheng Li,[ab] Yijun Cao[ab] and Jiang Liu*[ab]

As a clean and renewable energy source, the efficient production of hydrogen is crucial for the development of the hydrogen economy. Water electrolysis is an ideal route for green hydrogen production; however, the sluggish kinetics of the anodic oxygen evolution reaction (OER) severely limit the overall efficiency. Although precious metal catalysts exhibit excellent performance, their high cost and scarcity hinder large-scale applications. Despite the advantages of low cost and high stability that make Co_3O_4 a promising alternative, its catalytic performance still needs improvement. This study employed both alkaline chemical precipitation and acidic redox precipitation methods to successfully synthesize iron-doped cobalt oxide catalysts. Electrochemical measurements demonstrated that iron doping effectively enhances the oxygen evolution reaction performance of the material. It was further revealed that the sample prepared *via* the alkaline chemical precipitation method exhibited superior activity, requiring an overpotential of only 311 mV to achieve a current density of 10 mA cm^{-2} and displaying a Tafel slope of 85 mV dec^{-1}. Through a series of characterizations, it was confirmed that, compared to the acidic redox precipitation method, the iron-doped cobalt oxide catalyst prepared by the alkaline chemical precipitation method exhibits superior crystallographic structure. This structure effectively regulates the d-band center position, bringing it closer to the Fermi level, thereby enhancing the adsorption of oxygen-containing intermediates. This adjustment reduces the oxygen evolution reaction energy barrier and optimizes the reaction pathway. The combined optimization of the crystallographic structure and electronic structure significantly improves the electrocatalytic performance of the material and reduces mass transfer resistance during the reaction process.

Received 21st January 2026
Accepted 16th February 2026

DOI: 10.1039/d6ra00553e

rsc.li/rsc-advances

Open Access Article. Published on 27 February 2026. Downloaded on 4/2/2026 12:38:52 PM.
This article is licensed under a Creative Commons Attribution-NonCommercial 3.0 Unported Licence.

1 Introduction

At present, the global energy system is accelerating its transition toward a low-carbon and sustainable development paradigm centered on renewable energy. Driven by the dual imperatives of mitigating climate change and ensuring energy security, renewable energy sources such as solar and wind power have experienced rapid growth and have become key forces in promoting the green transformation of energy systems.[1] Meanwhile, continuous technological breakthroughs in emerging clean energy carriers, particularly hydrogen energy, are providing viable pathways for deep decarbonization in hard-to-abate sectors, including industry and transportation. As an integral component of clean energy systems, hydrogen energy is demonstrating considerable development potential. Owing to its high energy density, high conversion efficiency, and zero carbon emissions, hydrogen plays an irreplaceable role in industrial decarbonization, heavy-duty transportation, and long-term energy storage, where emission reductions are particularly challenging.[2,3] With the sustained decline in renewable energy costs, advances in water electrolysis technologies have created favorable conditions for the large-scale production of green hydrogen. Compared with hydrogen production from fossil fuels, water electrolysis uses water derived from non-fossil sources as the sole feedstock, producing only hydrogen and oxygen as products, without generating any by-products throughout the process.[4,5] In addition, the hydrogen produced by water electrolysis is characterized by high purity.[6] Consequently, among the various hydrogen production pathways, water electrolysis is regarded as an efficient and sustainable technology for hydrogen generation.

The overall water electrolysis process consists of two half-reactions: the hydrogen evolution reaction (HER) occurring at the cathode and the oxygen evolution reaction (OER) taking place at the anode.[7,8] As a four-electron transfer process, the OER involves a substantially more complex reaction mechanism than the two-electron HER and is therefore characterized by much slower reaction kinetics.[9] To achieve current densities and reaction rates comparable to those of the HER, the OER

[a]*Zhongyuan Critical Metals Laboratory and School of Chemical Engineering, Zhengzhou University, Zhengzhou, 450001, China. E-mail: liujiang2206@zzu.edu.cn*
[b]*Key Laboratory of Critical Metals Minerals Supernormal Enrichment and Extraction of Ministry of Education, Zhengzhou University, Zhengzhou, 450001, China*

© 2026 The Author(s). Published by the Royal Society of Chemistry

Open Access Article. Published on 27 February 2026. Downloaded on 4/2/2026 12:38:52 PM.
This article is licensed under a Creative Commons Attribution-NonCommercial 3.0 Unported Licence.

typically requires the application of a higher overpotential, which directly limits the overall efficiency of water electrolysis for hydrogen production.[7,10] Although noble-metal-based catalysts can effectively enhance the kinetics of both the HER and OER, thereby improving energy conversion efficiency, their large-scale practical application is severely constrained by resource scarcity, high cost, and stability issues.[7,11] Consequently, current research efforts have increasingly focused on the development of transition-metal-based electrocatalysts that combine high activity, high stability, and low cost.[12] Among these, cobalt-based catalysts offer several advantages, including tunable composition and structure, natural abundance, and relatively low cost. In particular, owing to their partially filled d orbitals, which can participate in chemical bonding, cobalt-based materials exhibit multiple accessible oxidation states and diverse chemical properties, endowing them with significant potential for OER catalysis and attracting widespread research interest.[13–16] Nevertheless, the intrinsic OER activity of Co_3O_4 remains far inferior to that of noble-metal oxides. The incorporation of metal elements such as Li, Ni, and Fe has been demonstrated to markedly enhance the OER catalytic performance of Co_3O_4.[17–20] Previous studies have shown that the introduction of Fe into cobalt-based oxide catalysts can effectively modulate their electronic structure, providing appropriate bonding strengths for oxygen-evolution intermediates and thereby reducing kinetic barriers associated with the OER.[21] Fe^{3+} preferentially substitutes Co^{3+} at the octahedral sites of the Co_3O_4 spinel lattice, inducing local lattice distortion and structural defects and forming Co–O–Fe linkages. These effects synergistically regulate the electronic structure of Co active sites, which is beneficial for the adsorption and transformation of oxygen-containing intermediates during the OER.[22,23] Meanwhile, the observed variations in Fe–O bond lengths and the reversible evolution of the Fe oxidation state under OER operating conditions suggest that Fe may not only act as an electronic modulator but may also directly participate in the catalytic reaction process.[24]

In the construction of Fe-doped Co_3O_4 electrocatalytic materials, precipitation methods represent one of the most commonly employed synthesis strategies. Among them, alkaline chemical precipitation and acidic redox precipitation constitute two fundamentally distinct precipitation pathways. The former relies on rapid nucleation and growth induced by OH^- species, which tends to generate open and hierarchical morphologies, whereas the latter is driven by redox-coupled reactions that promote cooperative precipitation, thereby favoring the formation of precursor structures with homogeneous compositional distribution and strongly coupled metal–oxygen frameworks.[25] Despite their widespread use, how these two representative precipitation pathways regulate structural evolution, electronic properties, and the resulting oxygen evolution reaction (OER) performance in Fe-doped Co_3O_4 systems remains insufficiently understood, and systematic, direct comparative studies are still lacking. Given the pronounced potential of Fe doping in enhancing the catalytic performance of Co_3O_4, the present study aims to elucidate the effects of different precipitation pathways on the structural evolution and OER activity of Fe-doped Co_3O_4 by systematically comparing alkaline chemical precipitation with acidic redox precipitation. Through a comprehensive comparative analysis of the catalysts prepared by these two methods in terms of their structural characteristics and electrocatalytic behavior, this work seeks to uncover the intrinsic origins of Fe-doping-induced enhancement in the OER activity of Co_3O_4, thereby providing experimental evidence and theoretical insights for the rational design and synthesis of efficient non-noble-metal OER electrocatalysts.

2 Materials and methods

2.1 Structural characterization of cobalt tetroxide

The X-ray diffraction (XRD) patterns and scanning electron microscopy (SEM) images of the as-prepared Co_3O_4 are presented in Fig. 1. As shown in Fig. 1a, a series of distinct diffraction peaks are observed at 2θ values of 18.97°, 31.29°, 36.85°, 38.57°, 44.81°, 55.44°, 59.34°, 65.15°, and 77.18°, which can be indexed to the (111), (220), (311), (222), (400), (422), (511), (440), and (533) crystallographic planes of cubic spinel Co_3O_4, respectively. These diffraction features are in excellent agreement with the standard Co_3O_4 pattern (JCPDS no. 42-1467; space group $Fd\bar{3}m$; lattice parameters $a = b = c = 8.084$ Å; $\alpha = \beta = \gamma = 90°$), confirming the formation of phase-pure Co_3O_4. Furthermore, the SEM images reveal that the sample exhibits a rod-like morphology, which is constructed from the aggregation of numerous nanosized primary particles.

To further elucidate the microstructural characteristics of the as-prepared Co_3O_4, Fourier transform infrared (FT-IR) spectroscopy and Raman spectroscopy were subsequently employed. As shown in Fig. 1c, the FT-IR spectrum exhibits two absorption bands located at 661 cm^{-1} and 562 cm^{-1}, which can be assigned to the stretching vibrations of Co^{3+}–O and Co^{2+}–O bonds, respectively, confirming the presence of a typical spinel structure. In addition, the Raman spectrum (Fig. 1d) displays five characteristic peaks at 185, 463, 502, 600, and 668 cm^{-1}, which can be indexed to the F_2g^1, E_g, F_2g^2, F_2g^3, and A_1g vibrational modes of Co_3O_4, respectively. These results are in

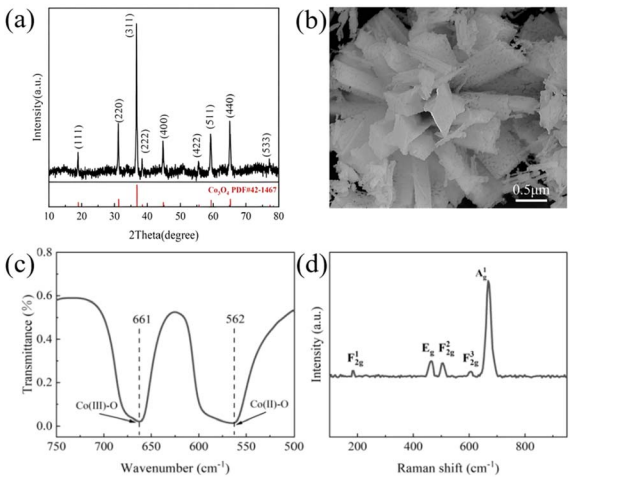

Fig. 1 (a) XRD pattern of Co_3O_4; (b) SEM image of Co_3O_4; (c) FT-IR spectrum of Co_3O_4; (d) Raman spectrum of Co_3O_4.

Open Access Article. Published on 4/2/2026 12:38:52 PM. This article is licensed under a Creative Commons Attribution-NonCommercial 3.0 Unported Licence.

excellent agreement with the reported Raman features of spinel Co_3O_4 in the literature.[26] The combined evidence from FT-IR and Raman analyses further demonstrates that the successfully synthesized sample is phase-pure Co_3O_4, rather than a mixed phase of CoO and Co_3O_4.

2.2 Structural characterization of FCO@A

To investigate the influence of the cobalt-to-iron feed ratio on the structure and performance of FCO@A materials prepared *via* the alkaline chemical precipitation method, the Co/Fe ratio in the precursor solution was systematically adjusted while all other experimental conditions were kept constant. The resulting samples were designated according to their corresponding cobalt-to-iron ratios as Co_3O_4, FCO@A-7, FCO@A-4, FCO@A-3, FCO@A-2, and FCO@A-1.

Fig. 2a presents the XRD patterns of FCO@A samples prepared with different amounts of iron precursor. No impurity phases are detected for any of the samples, indicating that all products possess a single spinel phase. Compared with pristine Co_3O_4, all diffraction peaks of the FCO@A samples exhibit an overall shift toward lower diffraction angles, suggesting that Fe^{3+} ions are successfully incorporated into the lattice and partially substitute for Co^{3+}, thereby inducing lattice expansion.[27] Meanwhile, with increasing Fe content, the diffraction peak intensity gradually decreases and the full width at half maximum (FWHM) increases, reflecting enhanced lattice distortion and structural disorder caused by iron incorporation, which in turn leads to reduced crystallinity. The FT-IR spectra shown in Fig. 2b further corroborate these structural changes. The Co–O vibrational bands associated with tetrahedral and octahedral sites, located at 661 and 562 cm^{-1}, respectively, shift toward lower wavenumbers after Fe doping. This behavior can be attributed to the substitution of Co^{3+} by Fe^{3+}, which results in an increase in metal–oxygen bond length or a weakening of bond strength, thereby altering the lattice vibrational modes. Collectively, these results confirm that iron has been successfully incorporated into the Co_3O_4 lattice and exerts a pronounced regulatory effect on its structure.

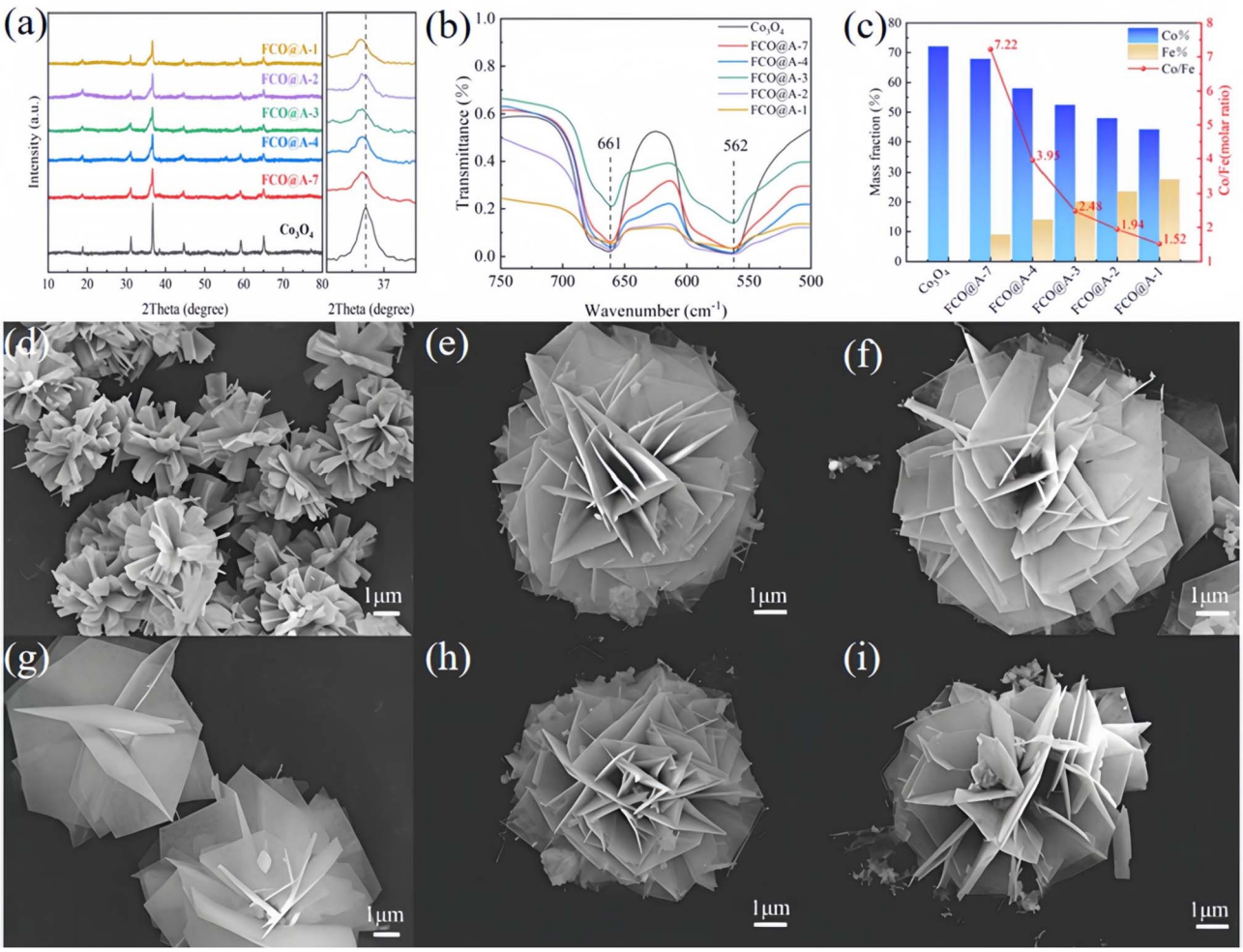

Fig. 2 (a) XRD patterns of FCO@A samples prepared with different Co/Fe ratios; (b) FT-IR spectra of FCO@A samples with different Co/Fe ratios; (c) mass percentages and corresponding molar ratios of Co and Fe in FCO@A samples synthesized with different Co/Fe ratios; (c) mass percentages and corresponding molar ratios of Co and Fe in FCO@A samples synthesized with different Co/Fe ratios; SEM images of FCO@A samples obtained at different Co/Fe ratios: (d) Co_3O_4, (e) FCO@A-7, (f) FCO@A-4, (g) FCO@A-3, (h) FCO@A-2, and (i) FCO@A-1.

© 2026 The Author(s). Published by the Royal Society of Chemistry

Open Access Article. Published on 27 February 2026. Downloaded on 4/2/2026 12:38:52 PM.
This article is licensed under a Creative Commons Attribution-NonCommercial 3.0 Unported Licence.

The microstructural morphologies of the samples are shown in Fig. 2d–i. Pristine Co_3O_4 exhibits a well-defined rod-like morphology, whereas with increasing Fe doping content, the material undergoes a pronounced morphological transformation. Within the Fe doping range of 0.2–1 mmol, all samples display a uniform petal-like architecture induced by the incorporation of iron. These observations indicate that the introduction of Fe not only modifies the lattice structure but also significantly influences crystal growth behavior, driving self-assembly along new directions into more open sheet-like or flower-like morphologies. Inductively coupled plasma optical emission spectroscopy (ICP-OES) analysis (Fig. 2c) reveals that the actual Co/Fe molar ratios of all samples are lower than the corresponding feed ratios, indicating that cobalt and iron hydroxides do not co-precipitate in a stoichiometric manner during the hydrothermal process. Owing to the substantial difference in the solubility products of cobalt and iron hydroxides, their precipitation kinetics differ, resulting in metal compositions in the final products that deviate from the initial design. Overall, the incorporation of iron plays a crucial role in lattice modulation, vibrational characteristics, and morphological evolution, thereby establishing a structural foundation for the subsequent enhancement of catalytic performance.

SEM-EDS and high-resolution transmission electron microscopy (HRTEM) analyses were employed to systematically characterize the elemental distribution and microstructural features of the FCO@A-3 sample. The SEM-EDS elemental mapping images shown in Fig. 3a reveal the presence of Fe, Co, and O elements with a homogeneous spatial distribution throughout the sample. Notably, the signal intensity of Fe is significantly lower than that of Co and O, providing preliminary evidence for the successful incorporation of iron into the Co_3O_4 lattice.

Further insight into the microstructural morphology and lattice structure was obtained from HRTEM analysis (Fig. 3b–e). The TEM images show that FCO@A-3 is composed of a large number of randomly aggregated nanoparticles with diameters of approximately 50–100 nm. Clear lattice fringes with an interplanar spacing of 0.249 nm are observed in the HRTEM image, which is slightly larger than that of the corresponding crystallographic plane in phase-pure Co_3O_4 (0.244 nm). This lattice expansion can be directly attributed to the substitution of Co^{3+} by Fe^{3+} ions with a larger ionic radius.[28] The corresponding elemental mapping images further confirm the homogeneous distribution of Co, Fe, and O at the nanoscale.

Collectively, the above results demonstrate that the uniformly Fe-doped FCO@A nanomaterials can be successfully synthesized *via* the alkaline precipitation method, and that Fe^{3+} ions are effectively incorporated into the Co_3O_4 lattice.

2.3 Structural characterization of FCO@B

To investigate the role of the cobalt-to-iron ratio in the formation of FCO@B materials prepared *via* the acidic redox precipitation method, the Co/Fe ratio in the reactants was systematically varied while all other synthesis parameters were kept constant. The obtained samples were designated according to their feed Co/Fe ratios as FCO@B-1, FCO@B-3, and FCO@B-6.

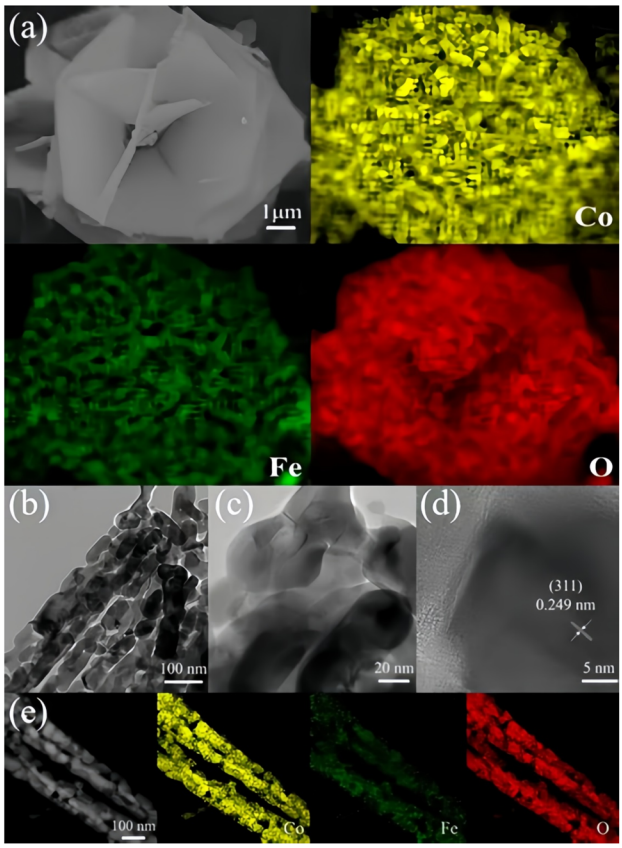

Fig. 3 (a) SEM image and corresponding elemental mapping of FCO@A-3; (b–d) TEM and HRTEM images of FCO@A-3; (e) HAADF-STEM image and corresponding elemental mapping of FCO@A-3.

Fig. 4a presents the XRD patterns of the FCO@B samples synthesized with different Co/Fe ratios under otherwise identical experimental conditions. As shown, when the Co/Fe ratios are 3 (FCO@B-3) and 6 (FCO@B-6), the diffraction peak positions of the products are essentially identical, and no characteristic peaks corresponding to other cobalt or iron oxide impurity phases are observed. In contrast, when the Co/Fe ratio decreases to 1 (FCO@B-1), the diffraction peaks of the product can be mainly indexed to the Fe_2O_3 phase. These results indicate that a low Co/Fe ratio is unfavorable for cobalt incorporation, leading to products dominated by Fe_2O_3, whereas increasing the cobalt content beyond a certain threshold induces a phase transformation to phase-pure Co_3O_4. FT-IR spectroscopy was further performed on the above samples, as shown in Fig. 4b. The samples with Co/Fe ratios of 3 and 6 exhibit characteristic absorption bands of spinel Co_3O_4 at 567 cm^{-1} and 659 cm^{-1}, which can be assigned to the vibrational modes of Co^{2+}–O and Co^{3+}–O bonds, respectively. By contrast, the sample with a Co/Fe ratio of 1 shows pronounced differences in both the positions and shapes of the absorption bands, indicating a distinct change in crystal structure. This observation is consistent with the XRD analysis and further confirms that Fe_2O_3 is the dominant phase formed under this condition.

The morphologies of the FCO@B samples synthesized at different Co/Fe ratios (1, 3, and 6) were further examined by

Open Access Article. Published on 27 February 2026. Downloaded on 4/2/2026 12:38:52 PM.
This article is licensed under a Creative Commons Attribution-NonCommercial 3.0 Unported Licence.

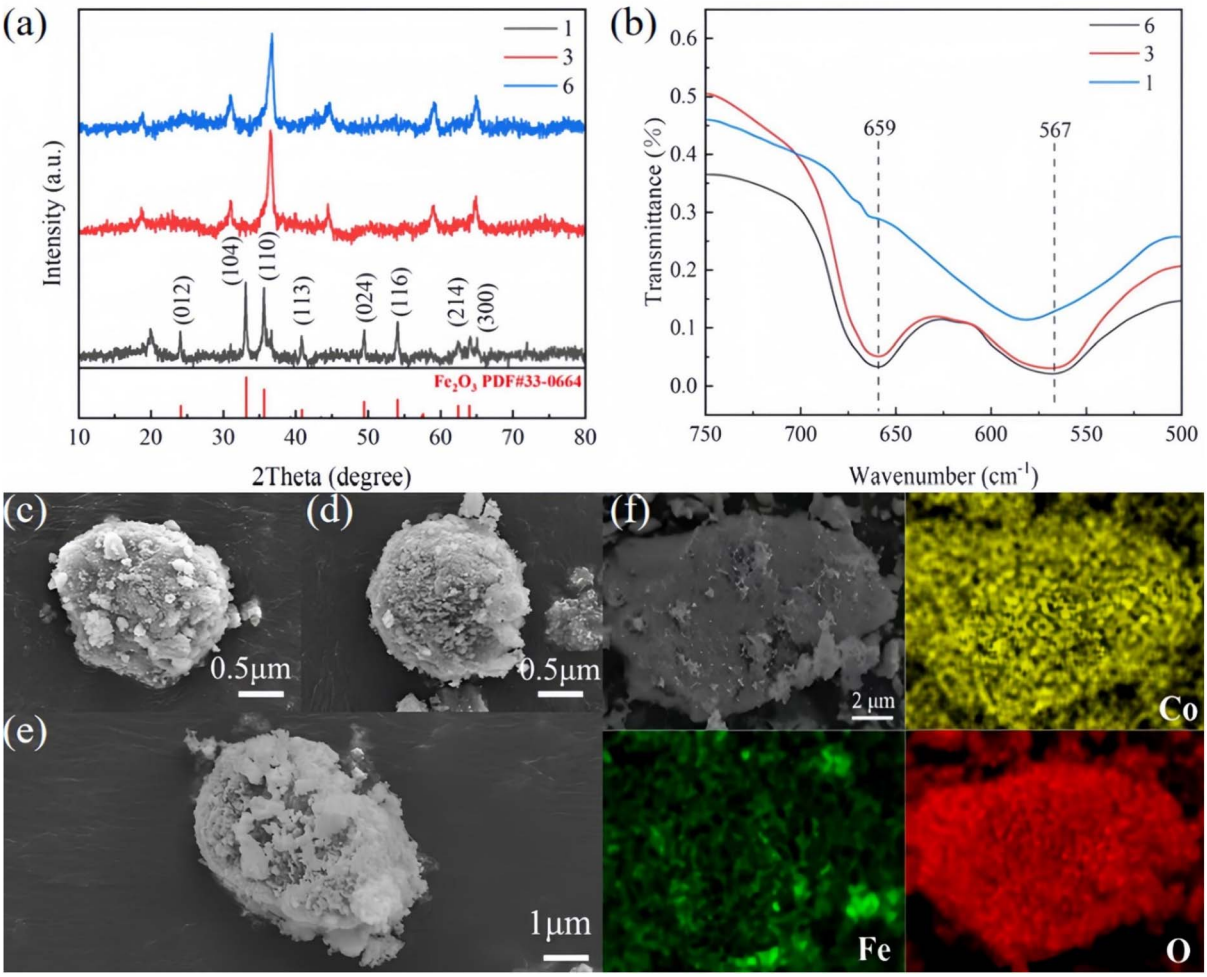

Fig. 4 (a) XRD patterns of FCO@B samples synthesized with different Co/Fe ratios; (b) FT-IR spectra of FCO@B samples prepared with different Co/Fe ratios; (c–e) SEM images of FCO@B samples obtained at different Co/Fe ratios: (c) FCO@B-1, (d) FCO@B-3, and (e) FCO@B-6; (f) SEM image and corresponding elemental mapping of FCO@B-6.

SEM, and the corresponding images are shown in Fig. 4c–e. The results reveal that all samples exhibit amorphous block-like morphologies, with no significant variation as a function of the precursor ratio, indicating that the Co/Fe ratio is not a key factor governing morphological evolution in this synthesis system. In addition, energy-dispersive X-ray spectroscopy (EDS) elemental mapping was conducted for the FCO@B-6 sample, as shown in Fig. 4f. Fe, Co, and O elements are homogeneously distributed throughout the sample, and the signal intensity of Fe is markedly lower than that of Co and O, further confirming that iron is successfully and uniformly incorporated into the Co_3O_4 lattice rather than forming a separate phase.

3 Results and discussion

3.1 Electrocatalytic oxygen evolution performance of FCO@A

Linear sweep voltammetry (LSV) measurements were conducted to evaluate the OER catalytic performance of different samples under identical conditions, and the results are clearly presented in Fig. 5a. Compared with pristine Co_3O_4, all Fe-doped Co_3O_4 samples exhibit markedly enhanced OER catalytic activity. The OER polarization curves recorded at a scan rate of 5 mV s^{-1} without *iR* compensation show that FCO@A-3 delivers the lowest OER overpotential of 311 mV at a current density of 10 mA cm^{-2}, which is substantially lower than those of Co_3O_4 (381 mV), FCO@A-7 (346 mV), FCO@A-4 (336 mV), FCO@A-2 (315 mV), and FCO@A-1 (317 mV). Notably, the OER catalytic activity initially increases and then decreases with increasing Fe content, indicating that an appropriate level of Fe doping is effective in reducing the OER overpotential of Co_3O_4.

The Tafel slope is a key parameter for evaluating the reaction kinetics of the electrocatalytic OER and can be directly derived from the LSV curves. As shown in Fig. 5b, the FCO@A-3 catalyst exhibits the lowest Tafel slope of 85 mV dec^{-1}, which is significantly smaller than that of pristine Co_3O_4 (100 mV dec^{-1}) and the other Fe-doped samples (FCO@A-7: 103 mV dec^{-1}; FCO@A-4: 93 mV dec^{-1}; FCO@A-2: 86 mV dec^{-1}; FCO@A-1: 87 mV dec^{-1}). A lower Tafel slope indicates that a smaller overpotential is required to achieve the same increment in

© 2026 The Author(s). Published by the Royal Society of Chemistry

Open Access Article. Published on 27 February 2026. Downloaded on 4/2/2026 12:38:52 PM.
This article is licensed under a Creative Commons Attribution-NonCommercial 3.0 Unported Licence.

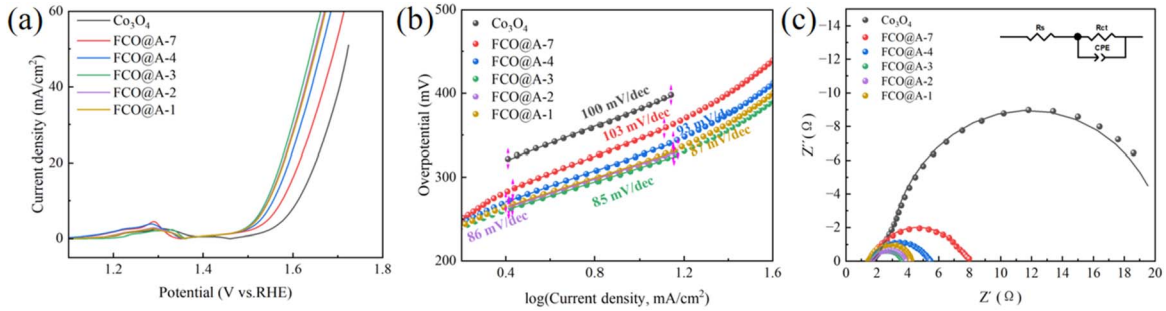

Fig. 5 (a) LSV curves and (b) corresponding Tafel plots of FCO@A samples with different Co/Fe ratios; (c) electrochemical impedance spectroscopy (EIS) Nyquist plots of FCO@A samples with different Co/Fe ratios, with the inset showing the fitted equivalent circuit.

current density, corresponding to faster reaction kinetics. These results further confirm that FCO@A-3 exhibits the most favorable OER kinetics and a more efficient reaction process.

Electrochemical impedance spectroscopy (EIS) measurements were conducted at an applied potential of 1.55 V, and the corresponding results are presented in Fig. 5c, with the fitted parameters of the equivalent circuit summarized in Table 1. The inset in the figure illustrates the equivalent circuit model employed, in which R_s, R_{ct}, and CPE represent the solution resistance, charge-transfer resistance, and constant phase element, respectively. As evidenced by the Nyquist plots, the FCO@A-3 electrode exhibits the smallest semicircle diameter, indicating the lowest charge-transfer resistance (R_{ct}) among the samples. The reduced R_{ct} value suggests that FCO@A-3 possesses superior electronic conductivity and faster interfacial reaction kinetics, which is consistent with its outstanding OER catalytic performance.

3.2 Electrocatalytic oxygen evolution performance of FCO@B

Fig. 6a shows the OER polarization curves of different FCO@B samples measured under identical testing conditions. The results indicate that FCO@B-6 requires an overpotential of 330 mV to reach a current density of 10 mA cm^{-2}, which is lower than those of FCO@B-3 (337 mV) and FCO@B-1 (348 mV), demonstrating its superior catalytic activity. The corresponding Tafel slopes are presented in Fig. 6b, where FCO@B-6 exhibits a value of 91 mV dec^{-1}, which is also lower than that of FCO@B-3 (95 mV dec^{-1}) and FCO@B-1 (98 mV dec^{-1}). A lower Tafel slope indicates faster reaction kinetics, further confirming the high efficiency of FCO@B-6 toward the oxygen evolution reaction.

Electrochemical impedance spectroscopy measurements were performed on the above samples at an applied potential of 1.55 V, and the corresponding results are shown in Fig. 6c. The impedance data were fitted using an equivalent circuit model, and the extracted parameters are summarized in Table 2. As can be seen, the FCO@B-6 sample exhibits a lower electrode resistance, which is consistent with the overpotential results.

Table 1 Electrochemical parameters of the equivalent circuit elements

Catalyst	R_s (Ω)	R_{ct} (Ω)	CPE-T	CPE-P
Co_3O_4	1.527	19.860	0.091914	0.89596
FCO@A-7	1.549	6.238	0.032370	0.72737
FCO@A-4	1.497	3.828	0.035649	0.70363
FCO@A-3	1.486	2.223	0.040972	0.68423
FCO@A-2	1.597	2.299	0.036401	0.68326
FCO@A-1	1.478	2.778	0.027324	0.80810

3.3 Comparison of electrocatalytic performance

In view of the pronounced differences in OER performance between the two Fe-doped Co_3O_4 materials revealed by the above electrochemical measurements, a systematic comparison was further conducted between the high-performing samples FCO@A-3 and FCO@B-6. As shown in Fig. 7a, the XRD diffraction peaks of FCO@A-3 synthesized *via* the alkaline chemical precipitation method exhibit significantly higher intensities than those of FCO@B-6 prepared by the acidic redox precipitation method, indicating a more complete crystal structure and a higher degree of crystallinity. Based on calculations using the integrated area method, the crystallinity of FCO@A-3 is determined to be 31.7%, whereas that of FCO@B-6 is only 16.6%, demonstrating that the former possesses higher crystallinity and a more ordered crystal structure. A comparison of the microstructural morphologies of FCO@A-3 and FCO@B-6 (Fig. 7b and c) further reveals pronounced structural differences between the two samples. FCO@A-3 exhibits a highly ordered petal-like architecture, whereas FCO@B-6 predominantly consists of amorphous block-like aggregates. This morphological disparity is likely closely related to the regulation of crystal growth mechanisms by Fe^{3+} doping during synthesis. Under alkaline chemical precipitation conditions, the incorporation of Fe^{3+} may alter the surface energies of different crystallographic planes and, in synergy with the selective adsorption of OH^- on specific facets, induce preferential crystal growth along certain directions, thereby giving rise to an open petal-like morphology. Such a structure is favorable for exposing more active crystal facets, increasing the specific surface area, and facilitating electrolyte penetration and gas bubble detachment, which collectively optimize the mass transport of reactants and products during the OER process.[29] By contrast, the

Open Access Article. Published on 27 February 2026. Downloaded on 4/2/2026 12:38:52 PM.
This article is licensed under a Creative Commons Attribution-NonCommercial 3.0 Unported Licence.

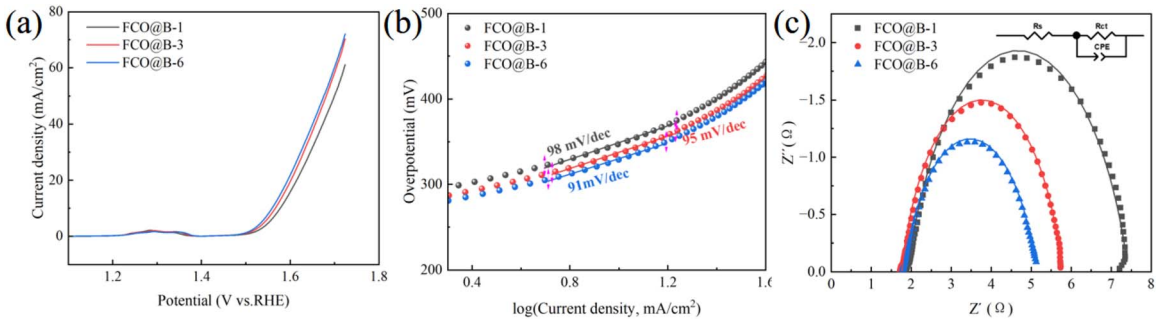

Fig. 6 (a) LSV curves and (b) corresponding Tafel plots of FCO@B samples synthesized with different Co/Fe ratios; (c) electrochemical impedance spectroscopy (EIS) Nyquist plots of FCO@B samples prepared with different Co/Fe ratios, with the inset showing the fitted equivalent circuit.

Table 2 Electrochemical parameters of the equivalent circuit elements

Catalyst	R_s (Ω)	R_{ct} (Ω)	CPE-T	CPE-P
FCO@B-1	1.912	5.516	0.016317	0.77746
FCO@B-3	1.792	4.005	0.016344	0.81922
FCO@B-6	1.819	3.306	0.017529	0.77977

acidic redox precipitation environment is unfavorable for anisotropic crystal growth, leading instead to the formation of relatively dense amorphous aggregates with limited accessibility of active sites. Consequently, the differences in morphology and structure jointly regulate the catalytic activity and reaction kinetics of the materials, further underscoring the critical role of the synthesis pathway in determining the final catalytic performance.

The position of the d-band center is commonly used as an important electronic-structure descriptor to evaluate the interaction strength between transition-metal-based catalysts and oxygen-containing intermediates (HO*, O*, and HOO*); however, its influence on catalytic activity should be interpreted within the framework of the Sabatier principle.[30] The valence band spectra (Fig. 7d) reveal that the d-band center of FCO@A-3 (−2.55 eV) is slightly shifted toward the Fermi level compared with that of FCO@B-6 (−2.66 eV), indicating that Fe doping under alkaline precipitation conditions effectively modulates the electronic structure of Co_3O_4. This moderate upward shift of the d-band center is conducive to enhancing the adsorption of oxygen-containing intermediates, thereby lowering the energy barriers of the oxygen evolution reaction, facilitating electron transfer, and promoting rapid charge transport.[31,32] Consequently, such electronic-structure regulation is considered beneficial for optimizing the energy-barrier distribution of

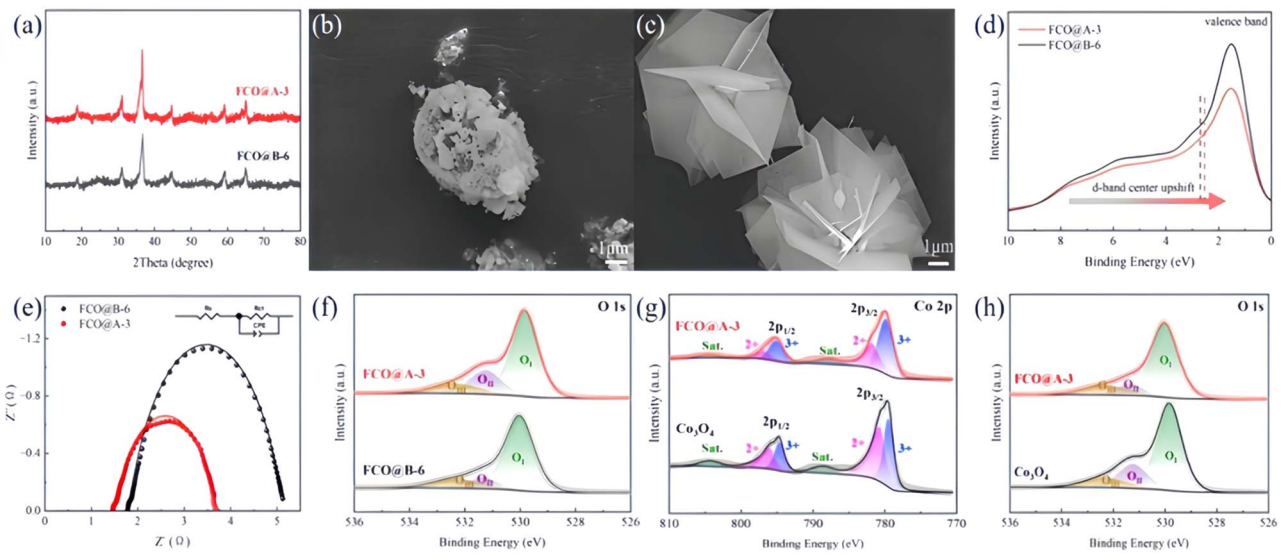

Fig. 7 (a) XRD patterns of FCO@B-6 and FCO@A-3; (b and c) SEM images of (b) FCO@B-6 and (c) FCO@A-3; (d) XPS valence band spectra and (e) electrochemical impedance spectroscopy (EIS) Nyquist plots of FCO@B-6 and FCO@A-3, with the inset showing the fitted equivalent circuit; (f) high-resolution O 1s XPS spectra and corresponding peak deconvolution results of FCO@B-6 and FCO@A-3; (g and h) high-resolution XPS spectra of FCO@A-3 and Co_3O_4: (g) Co 2p and (h) O 1s.

© 2026 The Author(s). Published by the Royal Society of Chemistry

Open Access Article. Published on 27 February 2026. Downloaded on 4/2/2026 12:38:52 PM.
This article is licensed under a Creative Commons Attribution-NonCommercial 3.0 Unported Licence.

multiple elementary steps involved in the OER process, thereby accelerating the overall reaction kinetics. It should be noted, however, that the d-band center serves only as a descriptive parameter reflecting trends in electronic-structure modulation, and its specific impact on OER activity ultimately depends on the synergistic balance among the adsorption energies of different oxygenated intermediates along the reaction pathway. Electrochemical impedance spectroscopy (EIS) results (Fig. 7e) further support this interpretation: the charge-transfer resistance of FCO@A-3 is only 2.223 Ω, which is significantly lower than that of FCO@B-6 (3.306 Ω), indicating more efficient interfacial charge transport. The O 1s XPS spectra (Fig. 7f) show that both samples consist of three components, namely lattice oxygen, defect oxygen, and adsorbed oxygen. Notably, the peak areas corresponding to O II and O III in FCO@A-3 are substantially increased, suggesting a higher abundance of surface-active oxygen species, including hydroxyl oxygen, adsorbed oxygen, and oxygen vacancies. Meanwhile, the O I peak maintains a relatively high intensity, indicating that the lattice structure remains largely intact. As a result, FCO@A-3 possesses a greater number of active sites and enhanced surface oxygen reactivity, which is favorable for improving the intrinsic OER activity.[28,33]

The Co 2p XPS spectra (Fig. 7g) further reveal the electronic-structure modulation induced by Fe doping. In FCO@A-3, the binding energies of the Co $2p_{3/2}$ and Co $2p_{1/2}$ main peaks are consistent with those of Co_3O_4 reported in the literature;[34–36] however, the integrated Co^{3+}/Co^{2+} ratio is markedly increased, indicating that the introduction of Fe elevates the average oxidation state of Co. This variation originates from electronic redistribution between Co and Fe, wherein electrons are transferred from Co to Fe, rendering the Co sites more prone to transformation into the catalytically more active CoOOH species during the OER process. A comparison of the O 1s spectra (Fig. 7h) shows that undoped Co_3O_4 possesses a higher concentration of oxygen vacancies, suggesting that oxygen vacancies are not the primary factor responsible for the enhanced conductivity induced by Fe doping. Overall, FCO@A-3 prepared *via* the alkaline chemical precipitation method outperforms FCO@B-6 in terms of d-band center regulation, charge-transfer capability, surface active oxygen species, and elevated metal oxidation states, thereby exhibiting superior intrinsic catalytic activity toward the oxygen evolution reaction.

To further elucidate the origin of the enhanced electrochemical activity, N_2 adsorption–desorption measurements were conducted for FCO@A-3 and Co_3O_4. As shown in Fig. 8a and b, both samples exhibit typical type IV isotherms, indicating the presence of mesoporous structures. Notably, FCO@A-3 possesses a significantly higher BET specific surface area (34.07 $m^2\ g^{-1}$) and pore volume (0.054 $cm^3\ g^{-1}$) than Co_3O_4 (17.66 $m^2\ g^{-1}$ and 0.0129 $cm^3\ g^{-1}$, respectively), along with a larger average pore size (6.79 *vs.* 5.06 nm). The larger specific surface area and more open pore architecture are conducive to exposing a greater number of active sites and enhancing mass transport efficiency, thereby improving the reaction kinetics of the oxygen evolution reaction.[37] Therefore, from a structural perspective, FCO@A-3 provides a more favorable catalytic

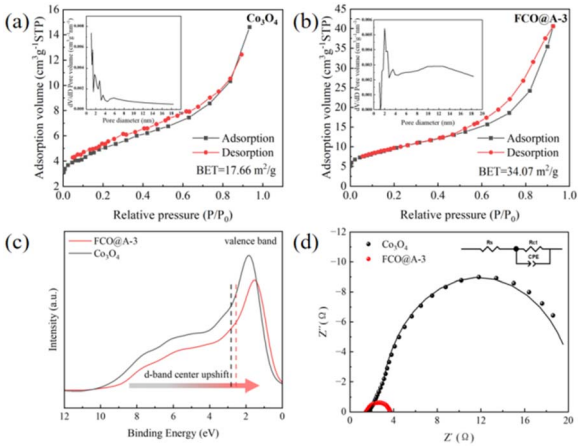

Fig. 8 (a) N_2 adsorption–desorption isotherms of Co_3O_4 and (b) FCO@A-3 (insets: corresponding pore size distributions); (c) XPS valence band spectra of Co_3O_4 and FCO@A-3, with the calculated d-band centers in the range of 0–10 eV; (d) electrochemical impedance spectroscopy (EIS) Nyquist plots of Co_3O_4 and FCO@A-3, with the inset showing the fitted equivalent circuit.

reaction environment and a higher density of accessible active sites than undoped Co_3O_4.

Valence band spectral analysis (Fig. 8c) further indicates that the d-band center of FCO@A-3 (−2.55 eV) is closer to the Fermi level than that of Co_3O_4 (−2.82 eV), suggesting that Fe doping enhances the interaction between the material and oxygen-containing intermediates. This electronic-structure modulation is favorable for lowering the energy barriers of the oxygen evolution reaction and accelerating electron transfer. Electrochemical impedance spectroscopy (EIS) results (Fig. 8d) show that the charge-transfer resistance of FCO@A-3 is only 2.223 Ω, which is substantially lower than that of Co_3O_4 (19.86 Ω), indicating superior charge-transport and electrical conductivity. Overall, the synergistic effects of structural optimization and electronic-structure regulation render FCO@A-3 superior to Co_3O_4 in terms of active-site utilization, interfacial charge transport, and adsorption of reaction intermediates, thereby resulting in enhanced intrinsic OER catalytic performance.

4 Conclusions

This study demonstrates that Fe doping is an effective strategy for enhancing the catalytic activity of Co_3O_4, and that the alkaline chemical precipitation method represents a key approach for the fabrication of high-performance Fe-doped Co_3O_4 catalysts. Systematic comparisons reveal that the alkaline chemical precipitation route offers pronounced advantages in constructing high-performance catalysts: the resulting FCO@A-3 sample (overpotential of 311 mV and a Tafel slope of 85 mV dec^{-1}) exhibits overall superior performance compared with the corresponding product prepared *via* the acidic redox precipitation method. Mechanistic investigations indicate that the alkaline environment not only enables effective incorporation of Fe but also synergistically optimizes the microstructural morphology, mesoporous architecture, and electronic

Open Access Article. Published on 27 February 2026. Downloaded on 4/2/2026 12:38:52 PM.
This article is licensed under a Creative Commons Attribution-NonCommercial 3.0 Unported Licence.

properties of the material. These combined effects expose a greater number of active sites, facilitate mass transport, and optimize the reaction pathway. Further analysis suggests that, during the alkaline precipitation process, the introduction of Fe^{3+} alters the surface energies of different crystallographic facets and induces preferential crystal growth, leading to the formation of a more open, petal-like hierarchical structure that is favorable for electrolyte penetration and rapid gas desorption. Meanwhile, electronic interactions between Fe and Co induce a moderate upward shift of the Co d-band center toward the Fermi level, thereby optimizing the adsorption strength of oxygen-containing intermediates and lowering the kinetic energy barriers of the oxygen evolution reaction. Overall, this work provides clear guidance and important experimental evidence for the rational design of efficient and cost-effective transition-metal-oxide OER electrocatalysts.

Author contributions

Jian Lv: writing – review & editing, writing – original draft, methodology, formal analysis. Hongtao Sun: writing – original draft, methodology, investigation. Cheng Li: writing – review & editing. Yijun Cao: resources, project administration, funding acquisition, data curation. Jiang Liu: writing – review & editing, funding acquisition, formal analysis.

Conflicts of interest

There are no conflicts to declare.

Data availability

The authors confirm that the data supporting the findings of this study are available within the article.

Acknowledgements

The authors are grateful for the financial support received from National Natural Science Foundation of China (52404301); Zhongyuan Critical Metals Laboratory (GJJSGFYQ202319); Open Fund project of Key Laboratory of Ecological Metallurgy of Multi-Metal Intergrown Ores of Ministry of Education (NEMM2022003); Henan provincial science and technology research and development program joint fund (232301420043); Henan Provincial Natural Science Foundation Outstanding Youth Fund (242300421061).

References

1 O. Ozkan, M. N. Coban and M. A. Destek, Navigating the winds of change: Assessing the impact of wind energy innovations and fossil energy efficiency on carbon emissions in China, *Renew. Energy*, 2024, **228**, 120623.
2 P.-A. Le, V. D. Trung, P. L. Nguyen, T. V. Bac Phung, J. Natsuki and T. Natsuki, The current status of hydrogen energy: an overview, *RSC Adv.*, 2023, **13**(40), 28262–28287.
3 U. Y. Qazi, Future of Hydrogen as an Alternative Fuel for Next-Generation Industrial Applications; Challenges and Expected Opportunities, *Energies*, 2022, **15**(13), 4741.
4 N. A. Khan, G. Rahman, T. M. Nguyen, A. U. H. A. Shah, C. Q. Pham, M. X. Tran and D. L. T. Nguyen, Recent Development of Nanostructured Nickel Metal-Based Electrocatalysts for Hydrogen Evolution Reaction: A Review, *Top. Catal.*, 2022, **66**, 149–181.
5 M. Chatenet, B. G. Pollet, D. R. Dekel, F. Dionigi, J. Deseure, P. Millet, R. D. Braatz, M. Z. Bazant, M. Eikerling, I. Staffell, P. Balcombe, Y. Shao-Horn and H. Schäfer, Water electrolysis: from textbook knowledge to the latest scientific strategies and industrial developments, *Chem. Soc. Rev.*, 2022, **51**(11), 4583–4762.
6 T. Terlouw, C. Bauer, R. McKenna and M. Mazzotti, Large-scale hydrogen production via water electrolysis: a techno-economic and environmental assessment, *Energy Environ. Sci.*, 2022, **15**, 3583–3602.
7 L. Fu, M. Liu, L. Ga and J. Ai, Advances of Ni-Based Electrocatalysts for Coupled Small Molecular Anodizing of Hydrogen from Electrolysis of Water, *Electroanalysis*, 2025, **37**(8), e70032.
8 K. S. Wagh, S. M. Mane, A. M. Teli, J. C. Shin and J. Lee, Recent Advancements in Co_3O_4-Based Composites for Enhanced Electrocatalytic Water Splitting, *Micromachines*, 2024, **15**(12), 1450.
9 T. Wu, M.-Z. Sun and B.-L. Huang, Non-noble metal-based bifunctional electrocatalysts for hydrogen production, *Rare Met.*, 2022, **41**(7), 2169–2183.
10 H. Li, J. Guo, Z. Li and J. Wang, Research Progress of Hydrogen Production Technology and Related Catalysts by Electrolysis of Water, *Molecules*, 2023, **28**(13), 5010.
11 G. Chen, W. Chen, R. Lu, C. Ma, Z. Zhang, Z. Huang, J. Weng, Z. Wang, Y. Han and W. Huang, Near-Atomic-Scale Superfine Alloy Clusters for Ultrastable Acidic Hydrogen Electrocatalysis, *J. Am. Chem. Soc.*, 2023, **145**(40), 22069–22078.
12 J. Han and J. Guan, Multicomponent transition metal oxides and (oxy)hydroxides for oxygen evolution, *Nano Res.*, 2022, **16**(2), 1913–1966.
13 M. Wtulich and A. Lisowska-Oleksiak, Tailoring TiO_2 nanotubes photoanodes with electrodeposited Co_3O_4 and CoOOH cocatalysts for enhanced electrocatalytic and photoelectrocatalytic oxygen evolution, *Appl. Surf. Sci.*, 2025, **714**, 164376.
14 Y. Song, Z. Du, C. Sun, L. Qiu, Y. Zhang, Y. Luan, X. Yang, J. Ma and H. Gao, Cobalt-Based Catalysts for Electrocatalytic Water-Splitting Reactions: Mini Review of Material Synthesis, HER, and OER Catalytic Performance, *ChemCatChem*, 2025, **17**(19), e00832.
15 M. Chen and J. Guan, Achievements and challenges in cobalt-based catalysts for water electrolysis, *Chem. Eng. J.*, 2024, **500**, 157080.
16 W. H. Lee, M. H. Han, Y.-J. Ko, B. K. Min, K. H. Chae and H.-S. Oh, Electrode reconstruction strategy for oxygen evolution reaction: maintaining Fe-CoOOH phase with

© 2026 The Author(s). Published by the Royal Society of Chemistry

Open Access Article. Published on 27 February 2026. Downloaded on 4/2/2026 12:38:52 PM. This article is licensed under a Creative Commons Attribution-NonCommercial 3.0 Unported Licence.

intermediate-spin state during electrolysis, *Nat. Commun.*, 2022, **13**, 605.

17 A. L. Silva, L. M. Esteves, L. P. C. Silva, V. S. Ramos, F. B. Passos and N. M. F. Carvalho, Mn-doped Co_3O_4 for acid, neutral and alkaline electrocatalytic oxygen evolution reaction, *RSC Adv.*, 2022, **12**, 26846–26858.

18 J. Liu, H. Sun, L. Wang, Y. Huang and Y. Cao, Magnetic field-assisted synthesis of iron-doped cobalt oxide with abundant oxygen defects as an electrocatalyst for oxygen evolution reaction, *J. Alloys Compd.*, 2025, **1013**, 178391.

19 R. A. Murugesan, K. Chandar Nagamuthu Raja, N. Devi, H.-T. Lin, C.-C. Huang, X.-Y. Jiang, Y.-Y. Li, G. Arthanareeswaran, L. Ponvijayakanthan, N. K. Jaiswal and Y.-S. Chen, Development of Ni-doped Co_3O_4 oxygen evolution catalysts for anion exchange membrane water electrolysis, *Int. J. Hydrogen Energy*, 2024, **72**, 677–686.

20 F. T. Dajan, Y. Wang, M. G. Sendeku, Y. Zhang, B. Wu, S. Hussain, M. Bahri, X. Zhan, Y. Li, X. Li and F. Wang, Dual Doping of Ruthenium and Iridium in Octahedral Sites of Spinel Co_3O_4 Nanoflowers for Enhanced PEM Water Electrolysis, *Small*, 2025, **21**(42), e09147.

21 Y. Liu, Y. Yan, F. Xu, L. Qiao, J. Sui, W. Cai and X. Zheng, Tuning the O p band center in Co_3O_4 catalysts by Fe doping for Switching lattice Oxygen-Mediated mechanism in Acidic oxygen evolution reaction, *Fuel*, 2025, **406**, 137224.

22 Y.-l. Chen, X.-w. Wang, W.-x. He, C. Yu, X.-j. Dang, Z.-y. Zheng and Y.-f. Zhang, Fe and Cr doped porous Co_3O_4@C nanosheets with abundant oxygen vacancies for highly efficient oxygen evolution reaction, *Mol. Catal.*, 2023, **548**, 113410.

23 A. El Jaouhari, J. Bencaid, A. Belhboub, M. Matrouf, I. Cheras, J. Zhu, B. Manoun and F. Ghamouss, Charge redistribution induced by well-dispersed cobalt oxide nanoparticles on $Co_3(PO_4)_2$ surfaces enhances OER catalytic activity, *Mater. Adv.*, 2025, **6**, 2956–2966.

24 F. T. Haase, E. Ortega, S. Saddeler, F.-P. Schmidt, D. Cruz, F. Scholten, M. Rüscher, A. Martini, H. S. Jeon, A. Herzog, U. Hejral, E. M. Davis, J. Timoshenko, A. Knop-Gericke, T. Lunkenbein, S. Schulz, A. Bergmann and B. Roldan Cuenya, Role of Fe decoration on the oxygen evolving state of Co_3O_4 nanocatalysts, *Energy Environ. Sci.*, 2024, **17**(5), 2046–2058.

25 C.-H. Yeh, W.-Y. Hsu, C.-C. Hsu, J. A. A. Valinton, C.-I. Yang, C.-c. Chiu and C.-H. Chen, Cobalt Iron Oxides Prepared by Acidic Redox-Assisted Precipitation: Characterization, Applications, and New Opportunities, *ACS Appl. Mater. Interfaces*, 2021, **13**(44), 52181–52192.

26 W. Shen, Q. Fu, C. S. Tsang, L. W. Wong, X. Zheng, J. Zhao and T. H. Ly, Facet-Junction Induced Strong Metal Support Interaction for Enhanced Alkaline Hydrogen Evolution Reaction, *Adv. Funct. Mater.*, 2024, **35**(21), 2406708.

27 S. Li, Y. Wang, J. Sun, Y. Zhang, C. Xu and H. Chen, Hydrothermal synthesis of Fe-doped Co_3O_4 urchin-like microstructures with superior electrochemical performances, *J. Alloys Compd.*, 2020, **821**, 153507.

28 Y. Su, B. Liu, Z. Shi, M. Yan and T. Ma, A Dual-Function Fe-Doped Co_3O_4 Nanosheet Array for Efficient OER and HER in an Alkaline Medium, *Molecules*, 2025, **30**(5), 1046.

29 M. Ayesha, S. Zeshan Ali, D. Muhammad, A. Rabia, S. Muhammad, R. Muhammad Asam, S. Aeysha, I. Munawar, M. A. Fatimah and M. Wissem, One-pot Hydrothermal Synthesis of Petal-like Pb_3O_4/CuO and Pb_3O_4/Co_3O_4 Nanostructures for High Performance Supercapacitor and Oxygen Evolution Reaction, *J. Inorg. Organomet. Polym. Mater.*, 2025, DOI: 10.1007/s10904-025-03965-4.

30 M. Zhang, K. Zhang, X. Ai, X. Liang, Q. Zhang, H. Chen and X. Zou, Theory-guided electrocatalyst engineering: From mechanism analysis to structural design, *Chin. J. Catal.*, 2022, **43**(12), 2987–3018.

31 Y. Miao, Q. Huang, D. Wen, D. Xie, B. Huang, D. Lin, C. Xu, W. Zeng and F. Xie, One-pot synthesis of NiFe nanoarrays under an external magnetic field as an efficient oxygen evolution reaction catalyst, *RSC Adv.*, 2023, **13**(7), 4249–4254.

32 Y. Fan, X. Hao, Y. Shao, Y. Wang and Z. Jin, Oxygen vacancy engineered electron structure of porous $CexCo_3{-}xO_4$ nanorods for wide spectrum photocatalytic hydrogen evolution, *Fuel*, 2023, **354**, 129337.

33 Q. He, L. Han and K. Tao, Oxygen vacancy modulated Fe-doped Co_3O_4 hollow nanosheet arrays for efficient oxygen evolution reaction, *Chem. Commun.*, 2023, **60**(9), 1116–1119.

34 J. Wang, D. Zhang, Y. Gao, F. Chen, T. Wang, H. Xia, X. Sui and Z. Wang, Fast-response hydrogen sulfide gas sensor based on electrospinning Co_3O_4 nanofibers-modified CuO nanoflowers: Experimental and DFT calculation, *Sens. Actuators, B*, 2023, **396**, 134579.

35 C. Han, X. Xu, H. Mu, Q. Tian, Q. Li, Y. Liu, X. Zhang, Z. Zhao and X. Su, Construction of hierarchical sea urchin-like manganese substituted nickel cobaltite@tricobalt tetraoxide core-shell microspheres on nickel foam as binder-free electrodes for high performance supercapacitors, *J. Colloid Interface Sci.*, 2021, **596**, 89–99.

36 S. Li, X. Qiu, X. An, E. Li, X. Li, G. Wang, P. Li, C. Shi, Y. Liu and G. Guan, Metal-organic framework derived spinel tricobalt tetroxide with trifle iridium sites for near-pH-neutral seawater electrolysis, *Chem. Eng. J.*, 2024, **491**, 151924.

37 C. Wang, G. Sui, D. Guo, J. Li, Y. Zhuang, W. Guo, Y. Zhou, X. Yang and D.-F. Chai, Inverted design of oxygen vacancies modulated $NiCo_2O_4$ and Co_3O_4 microspheres with superior specific surface area as competitive bifunctional materials for supercapacitor and hydrogen evolution reaction, *J. Energy Storage*, 2022, **49**, 104083.

© 2026 The Author(s). Published by the Royal Society of Chemistry